ACS OMEGA

Open Access

http://pubs.acs.org/journal/acsodf

Article

Mechanical and Viscoelastic Properties of Stacked and Grafted Graphene/Graphene Oxide−Polyethylene Nanocomposites: A Coarse-Grained Molecular Dynamics Study

Param Punj Singh and Raghavan Ranganathan*

Cite This: *ACS Omega* 2024, 9, 9063−9075

Read Online

ACCESS | Metrics & More | Article Recommendations | Supporting Information

ABSTRACT: High-performance natural materials with superior mechanical properties often possess a hierarchical structure across multiple length scales. Nacre, also known as the mother of pearl, is an example of such a material and exhibits remarkable strength and toughness. The layered hierarchical architecture across different length scales is responsible for the efficient toughness and energy dissipation. To develop high-performance artificial nacre-like composites, it is necessary to mimic this layered structure and understand the molecular phenomena at the interface. This study uses coarse-grained molecular dynamics simulations to investigate the structure−property relationship of stacked graphene−polyethylene (PE) nanocomposites. Uniaxial and oscillatory shear deformation simulations were conducted to explore the composites' mechanical and viscoelastic behavior. The effect of grafting on the glass-transition temperature and the mechanical and viscoelastic behavior was also examined. The two examined microstructures, the stacked and grafted GnP (graphene nanoplatelet)−PE composites, demonstrated significant enhancement in the Young's modulus and yield strength when compared to the pristine PE. The study also delves into the viscoelastic properties of polyethylene nanocomposites containing graphene and graphene oxide. The grafted composite demonstrated an increased elastic energy and improved capacity for stress transfer. Our study sheds light on the energy dissipation properties of layered nanocomposites through underlying molecular mechanisms, providing promising prospects for designing novel biomimetic polymer nanocomposites.

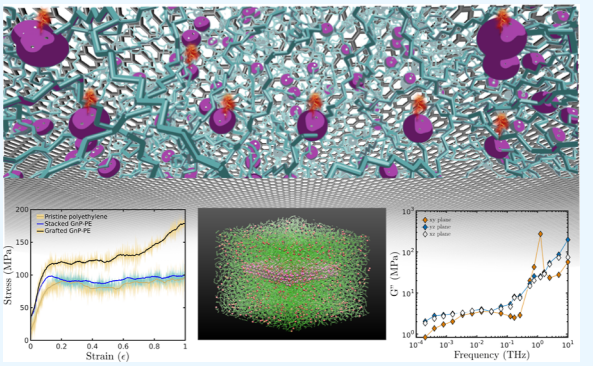

INTRODUCTION

With the continuous advancement of technology, the need for high-performance materials is increasing, which is crucial for addressing future challenges and promoting innovation across various fields.[1−10] In this regard, bioinspiration has played a significant role in developing new advanced materials with unique properties and functions. For instance, Nacre, commonly recognized as mother of pearl, possesses a distinctive staggered layered structure at both the nano- and micro-scales. On the nanoscale, millions of aragonite nanograins of 10−30 nm size are organized in layers, bonded by biopolymers. Meanwhile, at the micron length scale, these grains combine to form tablets of width 10−20 μm and 0.5 μm thickness, which are then arranged in a staggered pattern, glued together with biopolymers.[11] Inspired by the nacre's "brick and mortar" hierarchical structure, the layered polymer nanocomposites offer exceptional mechanical properties, making them useful in fields such as engineering, medicine, environmental applications, etc.[12−16] Polyethylene (PE), a thermoplastic polymer, is widely used in various industries due to its exceptional physical and chemical properties. Its lightweight, durability, flexibility, and ability to withstand harsh environmental conditions make it suitable for diverse applications.[17−19] On the other hand, graphene (Gr), a two-dimensional carbon material famous for its outstanding mechanical, thermal, and electrical properties, possesses a noteworthy Young's modulus of approximately 1 TPa, as well as elevated mechanical durability, formidable tensile strength (roughly 130 ± 10 GPa), and elasticity (allowing for up to 20% strain to failure.) .[20,21]

Earlier investigations on Gr and Gr-based polymer nanocomposites have indicated that incorporating Gr fillers at low levels (i.e., 1−4 wt %) into the polymer matrix can lead to polymer nanocomposites with superior thermal and mechanical properties.[22−24] Various experimental and simulation studies have provided ample evidence to indicate that various factors influence the mechanical and thermo-mechanical

Received: October 4, 2023
Revised: January 30, 2024
Accepted: February 6, 2024
Published: February 16, 2024

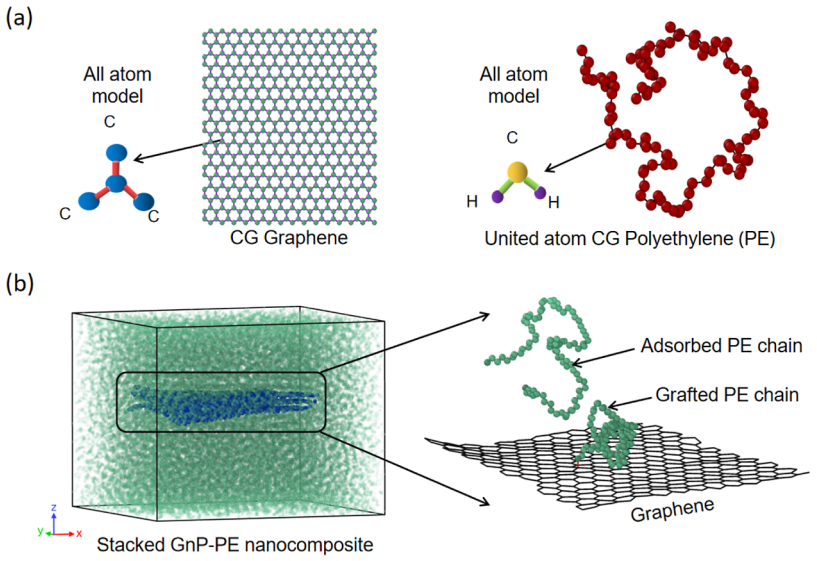

Figure 1. Schematic of (a) CG technique of the Gr and PE model, and (b) equilibrium snapshot of the GnP−PE composite, exhibiting adsorbed and grafted PE chains.

properties of nacre-like Gr-based composites. These include the chemical compatibility between the filler and the matrix,[25,26] their interactions, the volume fraction of the filler,[27,28] the mobility of polymer chains,[27,29] the chemical functionalization of nanoplatelets and cross-linking,[30] and the efficiency of stress transfer between the filler and the matrix.[31,32] Although the random distribution of Gr in a PE matrix can enhance the thermo-mechanical properties of Gr-based composites, the poor dispersion between Gr and the PE matrix leads to imperfect reinforcement.[33,34] Forming strong chemical bonds between the filler and the matrix is necessary to enhance interfacial interactions. This can be achieved by functionalizing nanofillers with covalent, ionic, or hydrogen bonding forces.[35−37] The planar arrangement of Gr nanoplatelets in the PE matrix through precoating and melt extrusion has demonstrated significant reinforcement (improvement in Young's modulus by 102%) in the direction along the planar orientation of Gr, surpassing that of randomly distributed Gr−PE composites.[38] Previous investigations into layered Gr−polymer nanocomposites have demonstrated a dependence on the number of layers and Gr size, concerning the mechanical properties of the composite. In the study of the Gr−polymethyl methacrylate composite, it was observed that below 2% volumetric concentration of Gr, the mechanical properties deviate from the actual properties. However, stability in properties was achieved after reaching a volumetric concentration of 2−3% Gr.[39] Several molecular dynamics (MD) investigations conducted on composites of Gr and PE have yielded a molecular-level understanding of the mechanical behavior and the strengthening effects of Gr reinforcement on PE.[36,40−43] Moreover, layered Gr-based polymer nanocomposites have shown great potential as materials with high impact-resistant properties. The layered arrangement of fillers naturally acts as a barrier to prevent crack propagation, thereby increasing the material's impact resistance and energy dissipation characteristics. Utilizing the MD technique, studies suggested that the layered arrangement of Gr in PE is one of the promising candidates for the development of lightweight, high-impact resistant, energy absorbing materials for ballistic impact and shock mitigation applications.[44−47]

The existing research on nacre-like Gr-based composites has significantly advanced our knowledge of material mechanics and viscoelasticity. However, understanding the interaction between Gr-based fillers and PE at the interface remains unclear. To address this issue, we studied to gain fresh insights into the mechanical and viscoelastic properties of coarse-grained (CG) stacked and grafted Gr nanoplatelet−polyethylene (GnP−PE) and graphene oxide−polyethylene (GO−PE) composite models. Our analysis includes evaluating the uniaxial tensile response and frequency-dependent dynamic moduli to understand the underlying deformation mechanisms. Our study's results are promising for structure−property analysis, and we anticipate that they may be valuable for refining these relationships and designing new Gr-based polymer nanocomposites. Ultimately, we aim to test these materials under extreme conditions, such as high-strain-rate impact and shock applications.

The structure of the article is as follows. The description of our simulation protocol and postprocessing methods for elucidating structure−property correlations is presented in Section 2. The main findings on tensile and viscoelastic behavior are presented in Section 3, and the conclusions are presented in Section 4.

COMPUTATIONAL METHODOLOGY

All simulations were carried out using the large-scale atomic/molecular massively parallel simulator (LAMMPS) package,[48] while OVITO 3.5.4[49] was employed for the visualization of the atomistic structures during deformation.

Preparation of the Stacked GnP−PE Nanocomposite. The nanocomposite used in the simulations consisted of the stacked CG Gr/GO filler and a PE matrix, as shown in Figure 1. A 4:1 CG scheme is employed for Gr, where four carbon atoms of all-atom Gr correspond to a single bead, as described in previous studies.[50,51] The CG PE follows the Drieding united-atom model CG scheme, where both CH_2 and CH_3 monomers are represented by a single bead.[52,53] Although various united-atom force fields, such as TraPPE, OPLS, PYS, CFF, etc., are actively used in the MD study of PE, the generic Drieding-UA force field is useful for predicting the structures

https://doi.org/10.1021/acsomega.3c07690
ACS Omega 2024, 9, 9063−9075

Table 1. Functional Forms and Force-Field Parameters for the CG-PE and Gr

types of interaction	functional forms and parameters (PE)	functional forms and parameters (GnP)
bond	$V_{bond} = k_b(r - r_o)^2$ K_b = 350 kcal mol^{-1}, r_0 = 1.53 Å K_{graft} = 350 kcal mol^{-1}, r_0 = 3.7 Å	$V_{bond} = D_0(1 - e^{-\alpha(d-d_0)})^2$ D_0 = 196.38 kcal mol^{-1} α = 1.55 Å^{-1}, d_0 = 2.8 Å
angle	$V_{angle} = K_\theta(\theta - \theta_0)^2$ k_θ = 30 kcal mol^{-1} rad^{-2}, θ_0 = 109.5°	$V_{angle} = K_\theta(\theta - \theta_0)^2$ k_θ = 409.40 kcal mol^{-1} rad^{-2}, θ_0 = 120°
dihedral	$V_{dihedral} = \sum_{i=0}^{3} k_i(1 - \cos(2\phi))$ k_1 = 4.49 kcal mol^{-1}, K_2 = 0.776 kcal mol^{-1} K_3 = 6.99 kcal mol^{-1}	$V_{dihedral} = k_\phi(1 - \cos(2\phi))$ k_ϕ = 4.15 kcal mol^{-1}
nonbonded	$V_{nb} = 4\epsilon_{LJ}\left[\left(\frac{\sigma}{r_{ij}}\right)^{12} - \left(\frac{\sigma}{r_{ij}}\right)^{6}\right]$ ϵ_{LJ} = 0.112 kcal mol^{-1}, σ = 4.01 Å	$V_{nb} = 4\epsilon_{LJ}\left[\left(\frac{\sigma}{r_{ij}}\right)^{12} - \left(\frac{\sigma}{r_{ij}}\right)^{6}\right]$ ϵ_{LJ} = 0.82 kcal mol^{-1}, σ = 3.46 Å

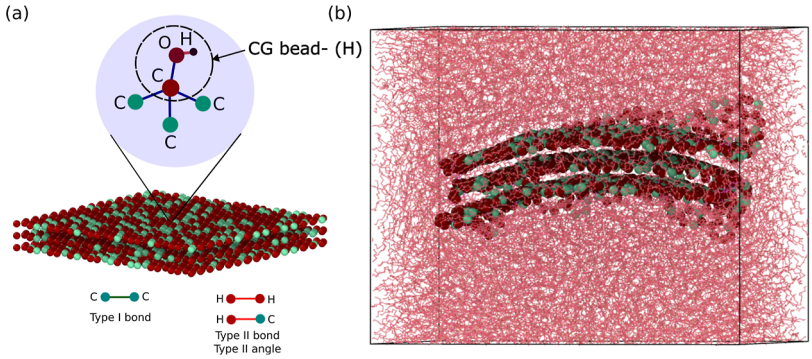

Figure 2. Schematic illustration of (a) 70% CG hydroxyl-functionalized GO. The functionalized CG−GO model comprises C−C (type I bond) and H−H/ H−C (type II bond and angle type). (b) Equilibrated snapshot of the GO−PE nanocomposite.

and dynamics of organic, biological, and main-group inorganic molecules. Though quantitative difference in the observed mechanical behavior may arise due to the choice of the force field, the Dreiding potential is expected to capture all the relevant nanoscale mechanisms originating from the polymeric phase. The bonded interactions were described by bond, angle, and dihedral interactions, while the nonbonded interactions were described by the Lennard-Jones potential, as outlined in Table 1. The cross-nonbonded interaction between Gr and PE was determined using the Lorentz−Berthelot mixing rules.[54]

The initial configuration was created by introducing a large simulation box containing a mixture of three layers of Gr stacked together and 100 monomer-long PE chains. Emphasizing the difference between infinite Gr flakes (periodic in both the x and y directions) and our finite Gr flake composite is crucial. Our structural inspiration is derived from the nacre architecture, wherein the hard phases are arranged in a stacked configuration and bound together by biopolymers surrounding the tablets. Periodic boundary conditions were applied in all three dimensions with a simulation time step set to 1 fs. For the grafted nanocomposite, the graft bond-creation process in LAMMPS involved generating bonds between the PE chains end and Gr beads within the cutoff distance of 3.7 Å. This distance mimics the equilibrium distance between PE and Gr beads in the context of their nonbonded interactions. This additional process for generating the grafted bonds was carried out at 800 K in an 800 ps NPT simulation. In the grafted GnP−PE composite, a grafting density (grafts/nm^2) of 4.46 was achieved, maintaining a harmonic bond interaction with a constant bond stiffness (K_{graft}) of 350 kcal mol^{-1} and an equilibrium bond length (r_0) of 3.7 Å, with no changes to angle and dihedral terms. The simulation box was then cooled from 800 to 300 K in a stepwise manner under the *NPT* ensemble at a 1 K/ps cooling rate. Subsequently, the stacked and grafted nanocomposite systems were equilibrated for 10 ns under the *NPT* ensemble at 300 K, during which the Gr flakes were tethered to the center of the simulation box to achieve the stacked configuration. During the equilibration period, the Gr was self-tethered with a spring force of 2 kcal mol^{-1}. The final dimension of the simulation box obtained after equilibration was 122 × 115 × 96 Å. The dimensions of the Gr flakes in the composite system were selected as 73 × 70 Å. Initially, the composite system's size was examined to assess the finite-size effect before proceeding with additional studies. The specifics of the finite-size effect are outlined in the Supporting Information (see Section S1). Figure 1 shows the equilibrated structures, with the permanent graft bonds shown in red.

Stacked and Grafted GO−Polymer (GO−PE) Nanocomposites. The CG GO model, as described by ref 55, preserves the hexagonal lattice structure of Gr through a 4:1 mapping scheme. The model used a type II bead (maroon color) to differentiate the oxidized functionalized group from type I Gr (green color) to represent 70% oxidation of Gr in the form of hydroxyl oxidized functional groups, as shown in Figure 2. In the CG−GO system, the nomenclature "C" and "H" refers to specific components within bonds and angles. Specifically, "C" represents carbon within the Gr structure, while "H" represents carbon that has been functionalized with hydroxyl groups in GO. Due to the introduction of distortion in the bond and angle terms due to the functional groups in Gr, the bond and angle of the nearest bead to the type II bead are substituted with the type II bond and angle, respectively.

https://doi.org/10.1021/acsomega.3c07690
ACS Omega 2024, 9, 9063−9075

The GO force field comprises bonded and nonbonded interactions, including bond, angle, and van der Waals' potential. The bond and angle interactions were modified to account for larger functional groups and their interaction with the nonoxidized carbon of Gr. The dihedral terms were taken as identical to Gr. The force field was optimized to accurately capture the in-plane properties of GO and the interlayer adhesion energies. The functional forms of the potential and modified parameters can be found in Table 2. Moreover, the nonbonded interaction between GO and PE is defined using the Lorentz−Berthelot mixing rule.

Table 2. Functional Forms and Force-Field Parameters for the CG-GO

types of interaction	functional forms and parameters (GO)
bond (type I)	$V_{bond} = D_0(1 - e^{-\alpha(d-d_0)})^2$
	D_0 = 443.07 kcal mol^{-1}, α = 1.154 Å^{-1}, d_0 = 3.7 Å
bond (type II)	$V_{bond} = K_b(d - d_0)^2$
	K_b = 317 kcal mol^{-1}, d_0 = 2.94 Å
angle (type I)	$V_{angle} = K_{angle}(\theta - \theta_0)^2$
	k_θ = 456.61 kcal mol^{-1} rad^{-2}, θ_0 = 120°
angle (type II)	$V_{angle} = K_\theta(\theta - \theta_0)^2$
	k_θ = 259.47 kcal mol^{-1} rad^{-2}, θ_0 = 120°
nonbonded	$nb = 4\epsilon_{LJ}\left[\left(\frac{\sigma}{r_{ij}}\right)^{12} - \left(\frac{\sigma}{r_{ij}}\right)^{6}\right]$
	ϵ_{I-I} = 0.0255 kcal mol^{-1}, ϵ_{II-II} = 0.128 kcal mol^{-1}, σ = 7.48 Å

The equilibration protocol used for the GO−PE nanocomposite was similar to that of GnP−PE, as discussed earlier. Grafting was performed between the PE chain ends and the oxidized Gr beads during equilibration. To investigate the impact of grafting on the viscoelastic properties of GO−PE nanocomposites, three sets of degrees of grafting (%), namely, 8, 36, and 60%, were employed.

Nonequilibrium Simulations. *Uniaxial Tension.* Equilibrated composite structures were subjected to uniaxial tensile deformation simulations, where the simulation box was deformed along one axis while keeping the pressure along the other two axes constant at P = 0 atm and 300 K. The effect of anisotropy was studied for each composite by extending the box along the X, Y, and Z axes under a fixed strain rate of 10^{10} s^{-1}. Five unique simulations of the individual systems were simulated for the statistical computation of the mechanical properties for each extension direction. Young's modulus, yield stress, and toughness were determined by analyzing the stress−strain profile up to an extension of 100%.

Oscillatory Shear Deformation. To investigate the frequency-dependent viscoelastic properties of the composites, an oscillatory shear deformation was applied,[56−58] and the resultant shear stress was analyzed. The equations of motion were integrated according to the SLLOD algorithm,[59,60] equivalent to the Lees−Edwards "sliding brick" boundary conditions. During the simulation, the simulation cell's planes were deformed along a particular shear system (denoted as xy, xz, or yz) at different frequencies. To calculate the temperature and thermostat, this velocity was subtracted from the velocity of each particle, resulting in a thermal velocity. The shear strain during the oscillatory shear deformation was determined by a sinusoidal function, which can be expressed as

$$\gamma_{xy} = \gamma_0 \sin(\omega t) \tag{1}$$

where γ_{xy} is the oscillatory shear amplitude and ω is the angular frequency. The virial shear stress,[61] which is also a sinusoidal function, can be expressed as follows

$$\tau_{xy} = \tau_0 \sin(\omega t + \delta) \tag{2}$$

where τ_0 is the shear stress amplitude and δ is the phase shift between the stress and the strain profile. The storage (G') and loss (G'') moduli and the loss tangent ($\tan\delta$) are calculated as follows

$$G' = \frac{\tau_0 \cos(\delta)}{\gamma_0} \qquad G'' = \frac{\tau_0 \sin(\delta)}{\gamma_0} \qquad \tan\delta = \frac{G''}{G'} \tag{3}$$

The shear frequency was adjusted within 5 MHz to 10 THz, while the shear strain amplitude (γ_o) was fixed at 0.012. Each system was simulated using nonequilibrium MD (NEMD) for 100 oscillatory shear cycles. The virial shear stress,[61] τ_{xy}, τ_{xz}, and τ_{yz}, was measured at intervals of every 10−100 time steps, and the stress response was averaged across the last 80 cycles to determine the viscoelastic behavior of the composites.

ANALYSIS

Bond Orientation Parameter. To determine the local structure of the chains, the bond orientation parameter $\langle P_2 \rangle$ defined by eq 4 was used to analyze the local PE conformation. During extension, conformational changes in the PE chains were calculated along the loading direction. The contribution of $\langle P_2 \rangle$ to the generated stress was due to the conformational entropy.[62]

$$\langle P_2 \rangle = (3\langle \cos^2\theta \rangle - 1)/2 \tag{4}$$

Here, θ is the angle between a bond vector and the stretching direction, and the notation $\langle\ \rangle$ represents the ensemble average over all the PE chains. $\langle P_2 \rangle$ can range from −0.5 to 1.0 for any given system. $\langle P_2 \rangle$ = −0.5 indicates a perfect perpendicular orientation to the loading direction, while $\langle P_2 \rangle$ = 0 corresponds to a random orientation. Finally, $\langle P_2 \rangle$ = 1.0 indicates a perfect alignment parallel to the loading direction.

Polymer Chain Relaxation and Vibrational Density of States. To consider the impact of polymer relaxation on energy dissipation, the structural relaxations of PE were investigated using the Rouse mode analysis. The Rouse model described the dynamics of PE chains of length N (in this case, N = 100) at an intermediate length/time scale. The Rouse modes (p), which correspond to distinct internal relaxations, were computed according to eq 5.[63−65]

$$\overrightarrow{X_p} = \left(\frac{2}{N}\right)^{1/2} \sum_{i=1}^{N} \vec{r}_i \cos\left[\left(\frac{p\pi}{N}\right)\left(i - \frac{1}{2}\right)\right] \tag{5}$$

The normal coordinates of the PE beads are represented by r_i, and the autocorrelation function of Rouse modes computed using eq 6 is expected to exhibit an exponential decay. The Rouse modes, which correspond to distinct internal relaxations of the polymer chain fragments of length N (in this case, N = 100), are typically independent and provide an estimate of the relaxation times for the chain fragments.

$$\langle \overrightarrow{X_p}(t) \cdot \overrightarrow{X_p}(0) \rangle = \langle \overrightarrow{X_p}^2 \rangle e^{-t/\tau_p} \tag{6}$$

https://doi.org/10.1021/acsomega.3c07690
ACS Omega 2024, 9, 9063−9075

During a production time of 100 ns, the coordinates of the beads were saved every 50 fs. The autocorrelation functions of the Rouse modes were then computed using the fast Fourier transformation algorithm.[66]

It is well known that in the harmonic approximation the power spectrum of the velocity correlation is the vibrational density of states (VDOS) as per eq 4.[56,65,67]

RESULTS AND DISCUSSION

Glass-Transition Temperature. The glass-transition temperature (T_g) of stacked and grafted Gr−PE nanocomposite is shown in Figure 3. To determine the T_g, the volume change was tracked as a function of temperature. The systems were cooled from 400 to 100 K at a rate of 1 K/ps, and the difference in the slope of the resulting curve indicated the T_g.

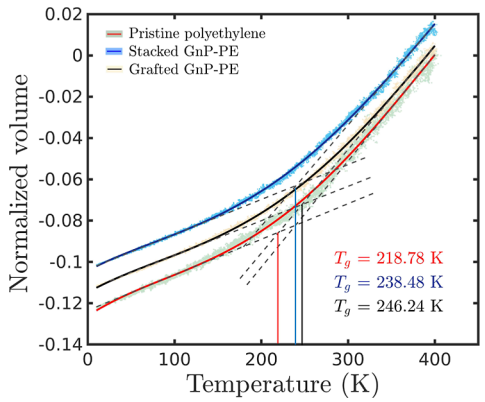

Figure 3. Plot of system volume as a function of temperature for the pristine PE, stacked GnP−PE, and grafted GnP−PE composite.

To ensure the accuracy of the computed T_g for the composite systems, the T_g of pure PE was also calculated, and its value was found to be consistent with previous studies.[68,69] The interface between Gr and PE influences the thermo-mechanical properties of nanocomposites. The shift in the T_g of the ungrafted and grafted systems indicates changes in the dynamics of PE near the stacked Gr. Grafting PE onto Gr flakes significantly reduces the mobility of the grafted and the adjacent freely adsorbed chains compared to the freely adsorbed PE chains in the stacked GnP−PE composite.

The shift in T_g of the nanocomposites is further supported by the computation of the monomer mean-square displacement (MSD) and PE's most prolonged relaxation mode (end-to-end distance autocorrelation function), as shown in Figure 4. It is to be noted that to study the PE dynamics in the stacked and grafted Gr, the Gr was tethered to its position with the help of a spring just for the aforementioned equilibrium MD analysis of MSD and end-to-end distance autocorrelation function. The MSD of PE monomers in the pristine system and the composite form is presented as a function of time at 300 K in Figure 4. The MSD curve of PE chains shows an initial ballistic regime ($\approx t^2$) for a short time scale. As time progresses, the transition from a subdiffusive regime ($\approx t^{0.5}$) to a diffusive regime ($\approx t^1$) is indicated. As evident from the graph, the gradient within the diffusive region implies that the diffusion coefficient of PE chains follows the sequence: pristine PE > stacked GnP−PE > grafted GnP−PE. The slow diffusion of PE chains in the presence of Gr is due to the attractive van der Waals interaction of the adsorbed PE chains at the interface, significantly reducing the chain mobility. In the grafted GnP−PE system, the PE chains grafted onto GnP serve as anchor sites, leading to increased rigidity in the PE matrix. This, in turn, results in a reduction in the mobility of the PE chains, as observed previously by Peng et al.[70] Furthermore, the time autocorrelation of the end-to-end distance of PE chains at 300 K is also shown in Figure 4, analogous to the result of chain diffusion. The time autocorrelation of Gr's PE chains shows the composite system's slow dynamics and larger relaxation time. In the presence of Gr flakes, PE exhibits a slower segmental relaxation, contributing to a higher T_g of the GnP−PE composites. Through the shape of the autocorrelation function, the graft-type composite exhibits a decay time larger than that of the ungrafted system.

Uniaxial Tensile Properties. The stress−strain behavior of GnP−PE nanocomposites in the lateral (x or y) and transverse (z) directions is compared in Figure 5, along with the mechanical behavior of pristine PE for comparison. The stress−strain characteristics of the PE system align with the findings from the earlier MD investigation by Hossain et al.[71] The Young's modulus and yield strength were determined to be 0.267 ± 0.023 GPa and 89.453 ± 2.145 MPa, respectively. The shaded region in the stress−strain plot is the standard

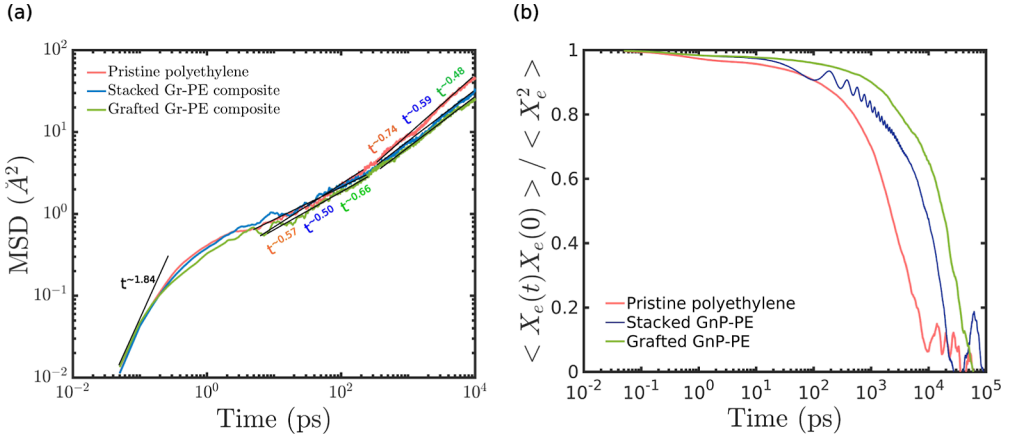

Figure 4. (a) MSD of the PE matrix and (b) end-to-end distance autocorrelation function of the pristine PE, stacked GnP−PE composite, and grafted GnP−PE composite.

https://doi.org/10.1021/acsomega.3c07690
ACS Omega 2024, 9, 9063−9075

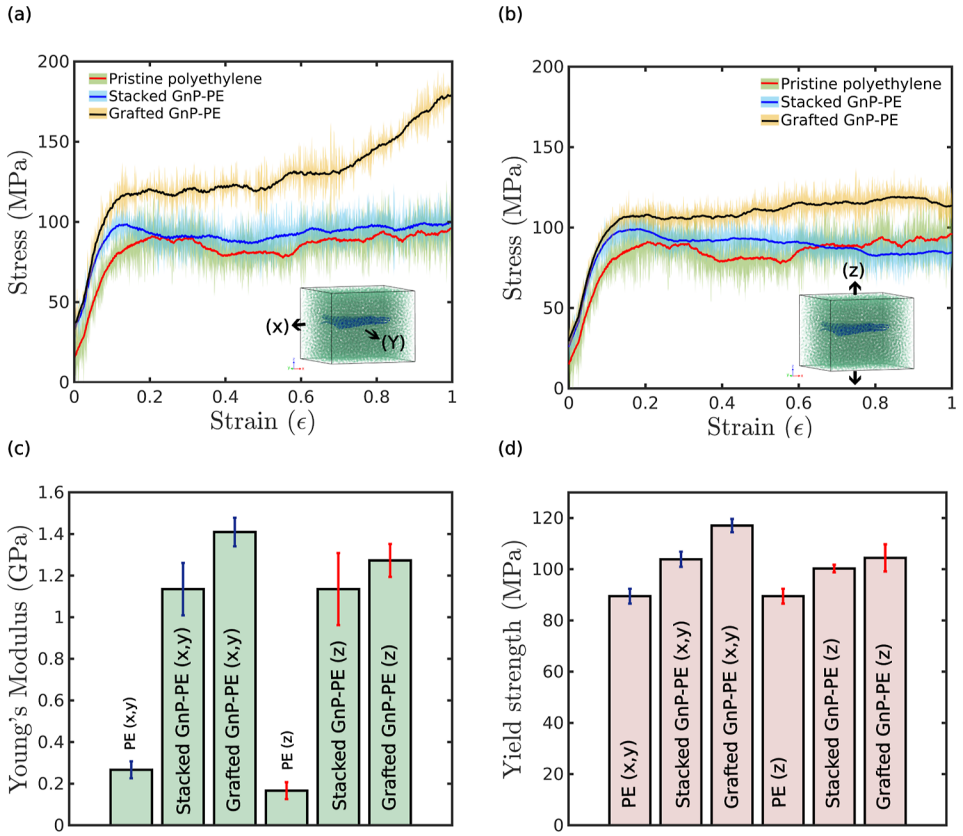

Figure 5. Stress−strain plot of pristine PE and the stacked and grafted GnP−PE nanocomposite for (a) lateral tensile extension and (b) transverse tensile extension. Bar plot of (c) Young's modulus and (d) yield strength of the nanocomposites with standard deviations.

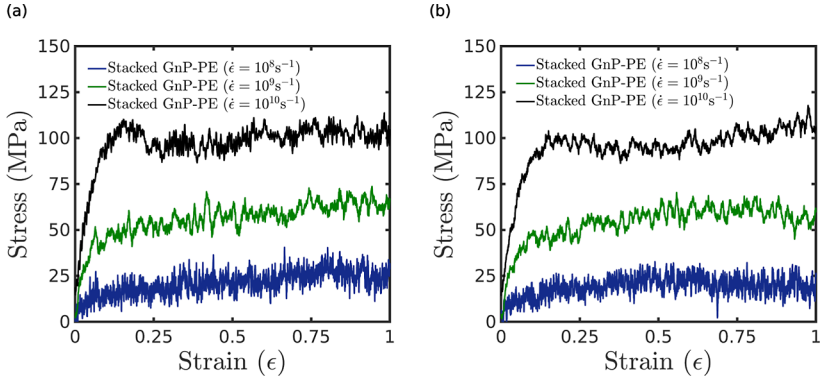

Figure 6. Strain rate response of the stacked GnP−PE systems for (a) lateral and (b) transverse extensions.

deviation for five unique simulations performed in the *x*, *y*, and *z* directions. The mean data of the simulations are shown as a solid line in the plot. The stress−strain plots exhibit the initial elastic deformation, followed by inelastic deformation for the nanocomposites studied. The stiffness of the stacked and grafted GnP−PE systems is observed to be significantly larger than that of the pristine PE due to the incorporation of Gr in PE. The Gr sheets are highly oriented and aligned along the *x*−*y* plane, giving rise to highly anisotropic properties in the composite material. The Young's modulus for the stacked and grafted GnP−PE systems in the lateral (*x*/*y*) direction is determined to be 1.148 ± 0.23 and 1.425 ± 0.145 GPa, respectively, as illustrated in Figure 5. Notably, the grafted system exhibits greater stiffness when extended in the lateral direction compared with the transverse direction. The yield strength exhibits a similar pattern with the grafted GnP−PE system, demonstrating the highest yield strength of 116 ± 3.15 MPa in the lateral direction. In contrast, the yield strength of the composite system showed a slight decrease in the transverse direction. The superior mechanical behavior is also due to the fact that grafting strengthens the interface and the adhesiveness of PE chains increases with the Gr. The details of the interfacial interaction between Gr and PE are outlined in the Supporting Information (see Section S2).

Effect of Strain Rate on Tensile Properties. In nanocomposite systems incorporating GnP−PE, tensile deformation was applied at strain rates of 10^{10}, 10^9, and 10^8 s^{-1}, respectively. Figure 6a,b displays the stress−strain curves for the stacked GnP−PE systems in both lateral and transverse directions for varying strain rates. The plot illustrates that as

https://doi.org/10.1021/acsomega.3c07690
ACS Omega 2024, 9, 9063−9075

the strain rate increases, the composites exhibit higher Young's modulus and yield strength. The variation of stress in the strain-hardening regime remains consistently constant, indicating similar molecular mechanisms involved in the process of tensile deformation in the lateral and transverse directions. Notably, the grafted GnP−PE system shows strain hardening, which is quite significant for lateral extension, as shown in the Supporting Information (see Section S3). The Young's modulus and the yield strength of the nanocomposite systems computed at different strain rates are given in Table 3. The

Table 3. Mechanical Properties of the GnP−PE Systems for Varying Strain Rates

system	strain rate (s^{-1})	$E_{x/y}$ (MPa)	E_z (MPa)	yield strength$_{x/y}$ (MPa)	yield strength$_z$ (MPa)
stacked	10^{10}	1207	1082	106	99
stacked	10^{9}	789	695	47	38
stacked	10^{8}	369	308	18	13
grafted	10^{10}	1383	1220	116	110
grafted	10^{9}	1068	992	61	49
grafted	10^{8}	480	476	21	17

enhanced stiffness and yield strength of the grafted GnP−PE are apparent during extension in all three directions. The grafting sites serve as a medium for efficient stress transfer from the matrix to the filler in the nanocomposite during deformation, thereby enhancing the overall strength and toughness of the composite.

Molecular Mechanisms Responsible for Tensile Behavior. The plots presented in Figure 7 depict the variations in the local PE conformation, characterized by the bond-orientation parameter $\langle P_2 \rangle$ and end-to-end distance, with respect to tensile strain in both the lateral and transverse directions.

The increase in $\langle P_2 \rangle$ and end-to-end distance is apparent as the PE chains align in the extension direction during tensile extension. However, in GnP−PE nanocomposites, PE conformational changes are constrained than in the pristine PE case. The plot clearly shows an initial isotropic local conformation in the PE chains in the pristine PE and the nanocomposites. In the process of extension, the PE chains within the grafted GnP−PE system exhibit a greater tendency for extension and reorientation. Furthermore, the alignment and reorientation of the PE chains are more prominent during extension in the lateral direction compared to the transverse direction. The significant difference in the orientational order parameter, $\langle P_2 \rangle$, observed in both lateral and transverse extensions of the grafted GnP−PE system signifies a highly ordered arrangement of PE chains during lateral extension. This organized alignment contributes to enhanced strength of the composite system. The notable difference in the mechanical strength, illustrated in Figure 5, directly corresponds to the observed phenomenon of chain reorientation during extension of the grafted GnP−PE system. Figure 7 illustrates the normalized end-to-end vector of PE chains as a function of the tensile strain. The PE chains exhibit significant elongation in the grafted GnP−PE system when extended in the lateral direction, resulting in a reduction in conformational entropy. This entropy decrease necessitates a higher energy input, indicative of the greater mechanical strength of the grafted system. Nevertheless, for the stacked GnP−PE system, the alterations in both $\langle P_2 \rangle$ and the normalized end-to-end distance of PE chains are negligible regardless of the extension direction, resulting in comparable strength.

For axial extensions, the shear mode is the major deformation mode. Therefore, the additional grafts enhance the polymer sliding resistance on the Gr interface, leading to enhanced stress transfer sites between the two phases. On the contrary, for the transverse extension, the opening mode of failure leads to chain crazing and delamination of polymer chains at the Gr interface. The yield strength of graft-type systems is improved significantly compared to that of ungrafted systems. Beyond the yield point, the GnP−PE nanocomposites exhibit a transition from strain-softening to strain-hardening behavior similar to that of the PE melt. A significant strain-hardening effect is observed in the grafted nanocomposite along lateral axes, as outlined in the Supporting Information (see Figure S3 a). The strength of the stacked Gr system is comparable to that of the pristine PE beyond elastic extension in contrast to that of the grafted composite. This is due to weak van der Waals interactions between Gr and PE, which cannot withstand increasing strain, resulting in PE chain delamination at the interface. In contrast, the grafted composite exhibits enhanced tensile strength during in-plane extension due to enhanced stress transfer sites, as observed in the atomistic snapshot, as shown in Figure 8. In lateral extension, Gr flakes are noted to retain their planar orientation, whereas under transverse loading the Gr flakes readily undergo

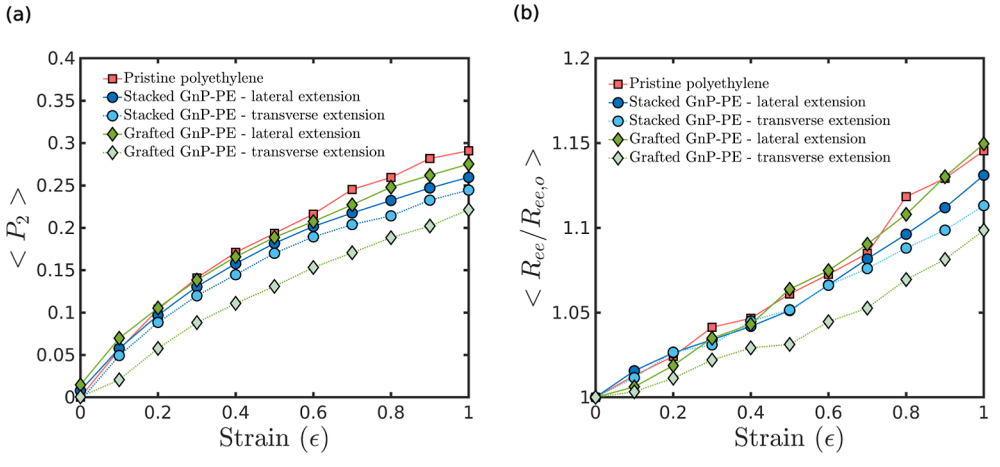

Figure 7. (a) Bond-orientation parameter $\langle P_2 \rangle$ and (b) normalized end-to-end distance of PE as a function of strain.

https://doi.org/10.1021/acsomega.3c07690
ACS Omega 2024, 9, 9063−9075

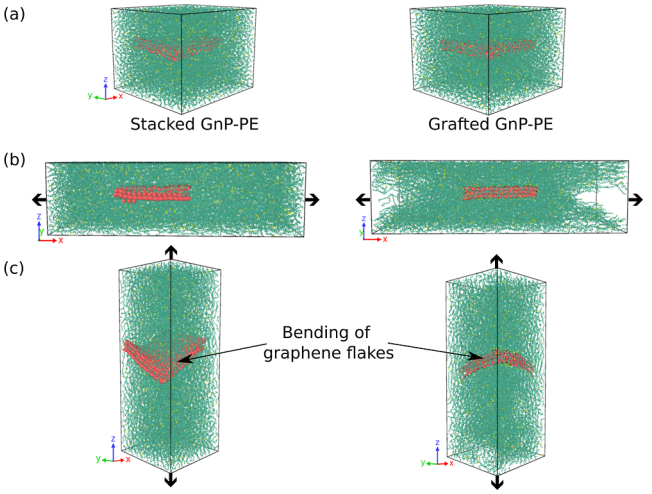

Figure 8. Snapshots of tensile deformation of the (a) stacked and grafted GnP−PE nanocomposite in (b) lateral (x/y) and (c) transverse (z) directions at 100% strain.

bending in response to the applied load. The Gr's greater tensile rigidity over its flexural stiffness aligns with the variations in the mechanical strength of the composites in distinct directions. However, the exceptional flexibility of Gr contributes to the overall strength of PE chains, making it susceptible to withstand loads without breaking.

Frequency-Dependent Viscoelastic Behavior. Here, the dynamic moduli of GnP−PE nanocomposites vary with the oscillating shear frequency, which was between 5 MHz and 10 THz. Figure 9 illustrates the viscoelastic behavior of the nanocomposites in comparison to that of pure PE.

The storage modulus (G'), loss modulus (G''), and tan δ of the GnP−PE nanocomposite were found to be higher than that of PE melts across the frequency range. The enhanced elastic response of the composites is due to the interaction of Gr and PE and the PE chain relaxation modes at frequencies <0.3 THz. In such low frequencies, the energy storage is attributed to the slow variation in PE chain conformation (chain relaxation) and the sliding of intergraphene flakes. At frequencies greater than 0.3 THz, the energy storage is majorly attributed to the vibrational modes of Gr and PE. As the frequency increases, the PE chains become more rigid, increasing the elastic behavior. In addition, the loss modulus (G'') is an indicator of stress dissipation and is influenced by different phases present at varying time scales, as shown in Figure 9. At frequencies below 0.3 THz, stress relaxation occurs through the relaxation of chain fragments, also known as Rouse modes, over increasingly longer time scales. At this range, the G'' of GnP−PE nanocomposites is similar to that of PE melts due to the higher volumetric fraction of PE chains in the composites that contributes to stress dissipation. At higher frequencies, between 0.3 and 10 THz, the behavior of the loss modulus is dominated by vibrational modes and intermolecular interactions. Molecules have less time to relax at this range, and the increase in G'' is attributed entirely to van der Waals interactions.

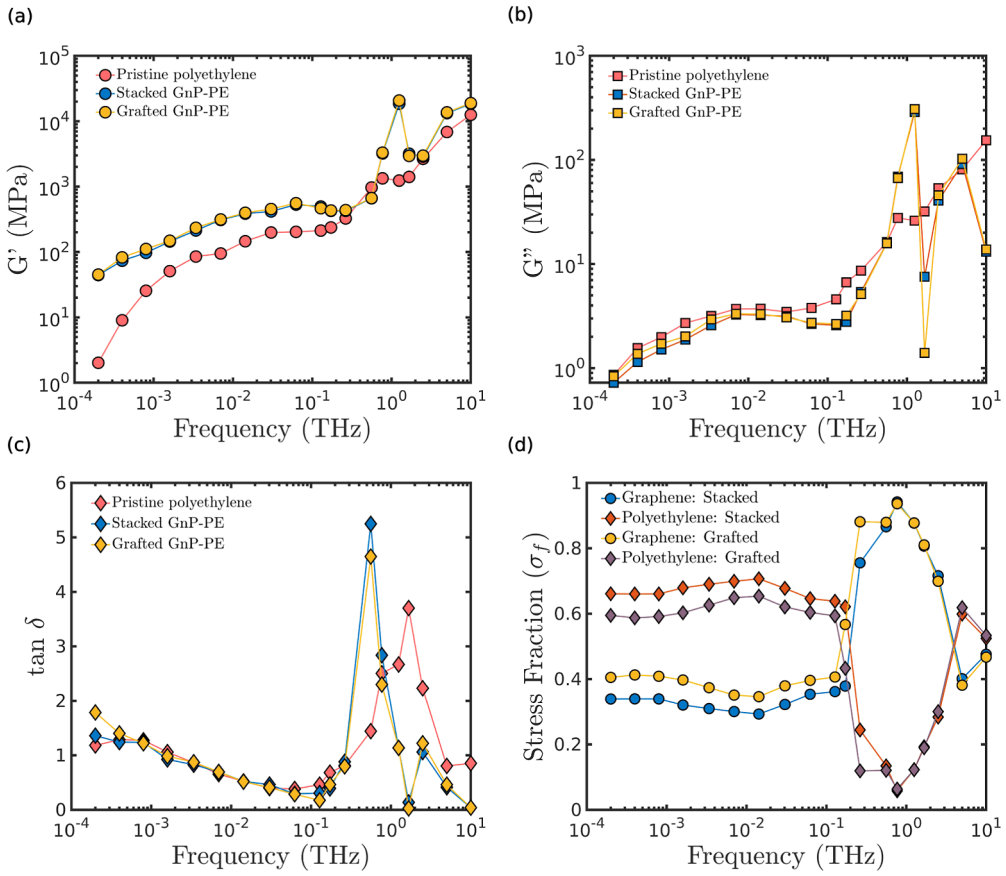

Figure 9. (a) Storage modulus, (b) loss modulus, (c) tan δ, and (d) stress distribution fraction for Gr and PE domain for the stacked and grafted GnP−PE nanocomposites.

https://doi.org/10.1021/acsomega.3c07690
ACS Omega 2024, 9, 9063−9075

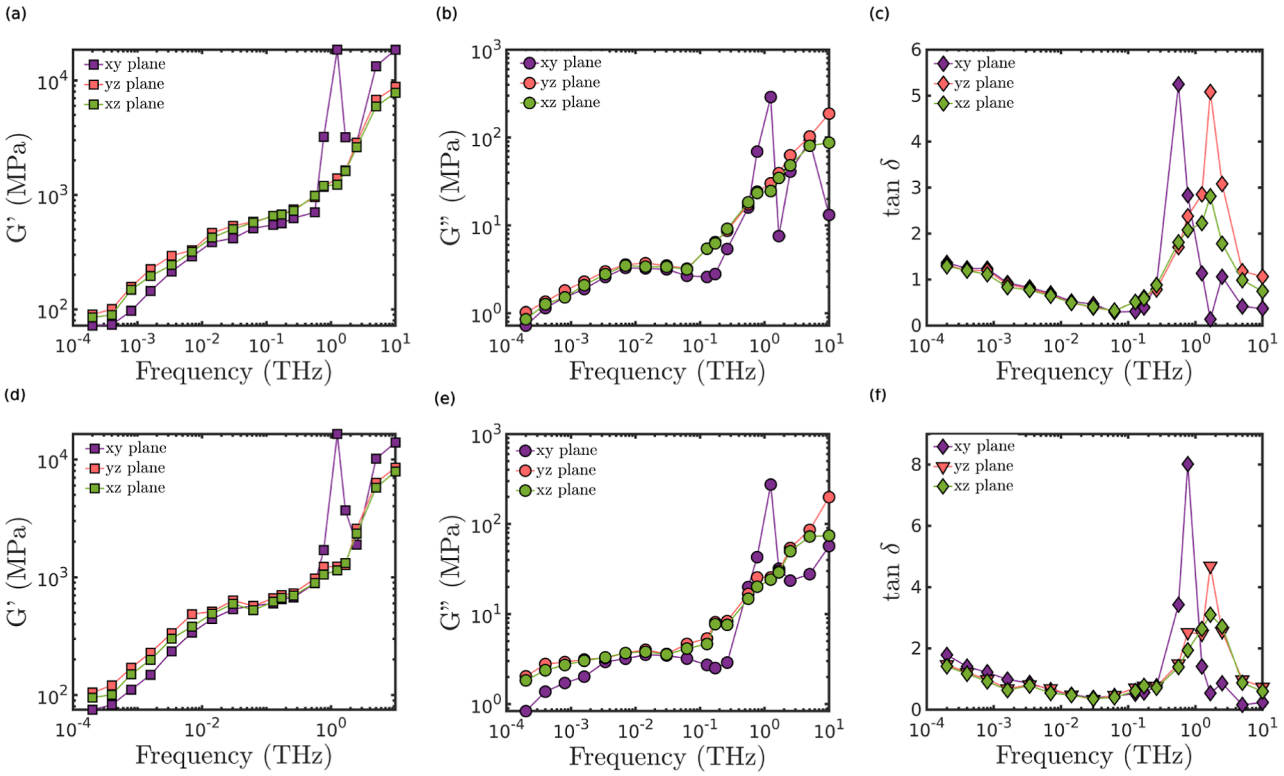

Figure 10. (a,d) Storage modulus, (b,e) loss modulus, and (c,f) tan δ for varying shear systems in the stacked and grafted GnP−PE nanocomposites.

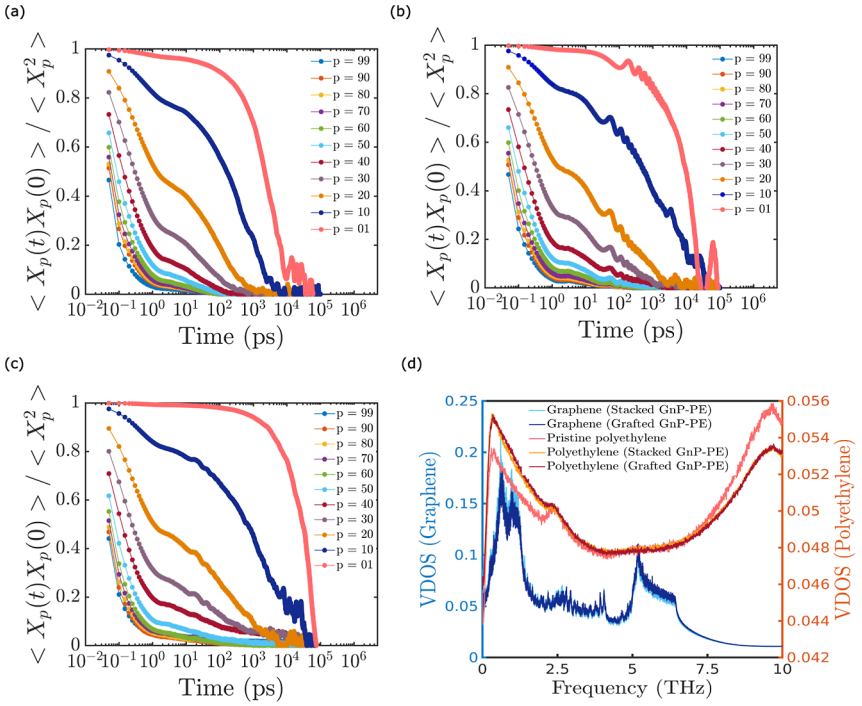

Figure 11. Rouse modes (p = 99, 90, 80, 70, 60, 50, 40, 30, 20, 10, and 01) for the (a) pristine PE, (b) stacked GnP−PE nanocomposite, and (c) grafted GnP−PE nanocomposite at T = 300 K. The autocorrelation function is normalized to scale the characteristic time scale. (d) Comparison of the partial VDOS of Gr and PE for the nanocomposites.

The composite with improved dissipation displays a significant peak in G' and G'' at approximately 1 THz. Both G' and G'' increase by about 20 times compared to pristine PE. The GnP−PE nanocomposite exhibits a prominent peak in tan δ at a frequency of around 0.3 THz. The phase difference of the GnP−PE composite shows a remarkable 45% increase compared to the PE melt. The grafted composite exhibits slightly higher G' and G'' than the stacked GnP−PE composite across the investigated frequency range.

https://doi.org/10.1021/acsomega.3c07690
ACS Omega 2024, 9, 9063−9075

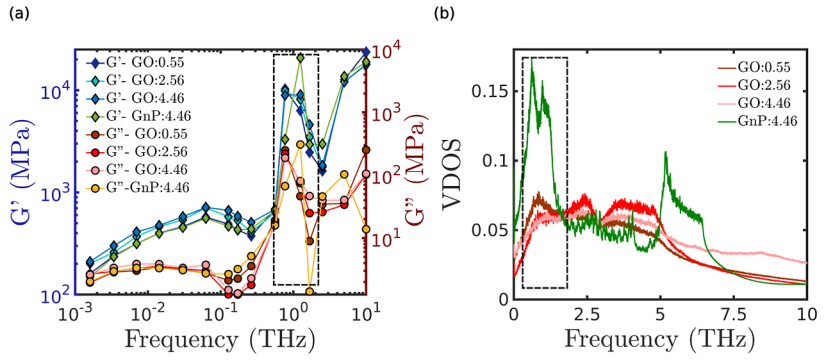

Figure 12. (a) Comparison of G' and G'' of the GnP/GO−PE nanocomposite for varying grafting densities and (b) VDOS spectra for Gr and GO in varying degrees of grafted GO−PE nanocomposite.

To analyze the frequency-dependent stress response of the composite systems, we calculated the fraction of shear stress (σ_f) borne by PE and Gr. The PE chains carry the overall shear stress for the lower frequency range, as they undergo slow conformational changes. However, Gr exhibits a higher contribution, ≈1.5 times the shear stress at the frequencies of maximum dissipation. Additionally, grafting increases the stress contribution of Gr in the grafted nanocomposite, resulting in a higher value of the stress fraction for the grafted Gr than for the stacked Gr system.

Orientation-Dependent Viscoelastic Behavior. The layered arrangement of Gr flakes gives rise to anisotropic characteristics, often manifesting distinct mechanical and viscoelastic properties along different axes. This anisotropy plays a pivotal role in influencing the material's response to shear forces, contributing to varied shear moduli in different orientations. Figure 10 illustrates the directional dependence of the viscoelastic behavior of the nanocomposites subjected to varying shear deformation directions, namely, *xy*, *yz*, and *xz* studied for the same GnP−PE structures.

The storage and loss moduli of the stacked and grafted GnP−PE composite exhibit an increase with increasing shear frequency, as illustrated in Figure 10a,b,d,e). Notably, the *yz* axis shear in the composite system demonstrates higher G' and G'' compared to shear along the *xz* and *xy* directions for both composites below 0.8 THz. Deformation along the *xz* and *yz* directions revealed PE as the carrier of shear stress in the composites. For frequencies above 0.8 THz, the moduli for *xy* shear show enhancement. This phenomenon can be attributed to the heightened stress-carrying capability of Gr flakes at these frequencies, as explained in the Supporting Information (see Section S4). In the frequency range of 0.8−2 THz, Gr exhibits a cyclic pattern of significant stress dissipation when subjected to deformation in a plane parallel to its orientation. Nevertheless, the difference in moduli is insignificant for the rest of the lower-bound frequencies, primarily because of the low volume fraction of Gr within the PE matrix. The noticeable difference in the G' and G'' for *yz* and *xz* shear deformations is primarily attributed to the anisotropic characteristics of Gr's armchair and zigzag edges, respectively. Figure 10c,f depicts the discrepancy in phase lag within the composite system. Notably, the deformation along the *xz* and *yz* planes demonstrates maximum energy dissipation at a higher frequency, highlighting the frequency-dependent nature of energy dissipation. This divergence is attributed to the Gr stress-carrying capacity in the *xy* shear system at relatively lower frequencies. Conversely, at higher frequencies, where the *xz* and *yz* shear systems exhibit the highest dissipation, it is attributed to the stress-carrying capacity of the PE component in the composite system. This phase difference is notably more pronounced in the stacked GnP−PE system compared to the grafted composite.

Molecular Mechanisms Responsible for Viscoelastic Behavior. Figure 11a−c shows the Rouse mode relaxation of the PE melt, stacked GnP−PE nanocomposite, and grafted GnP−PE nanocomposite, respectively.

In general, the Rouse modes (p = 1, 2, 3, ⋯, N − 1) describe the stress relaxation of a system at multiple time scales. These overall relaxation spectra comprise the shortest to longest relaxation modes, exhibiting the exponential decay characterizing the Rouse relaxation time of each mode. Comparing the decay time, the grafted GnP−PE system shows a longer relaxation time than those of the stacked GnP−PE and the PE melt. For the Rouse modes, p = 99 to 40, the characteristic relaxation time (inverse of 0.01−1 THz) correlates well with the maximum stress dissipation peaks for the composites, as shown in G'' and tan δ plot (Figure 9).

The partial VDOS values shown in Figure 11 for Gr and PE are computed for the composites to investigate the vibrational modes of stress dissipation. At higher frequencies, relative sliding and vibration of atoms contribute to the stress dissipation mechanism in the materials. The prominent VDOS peaks observed for both phases corroborate with the maximum damping frequency of the composites at the frequency range of 0−5 THz. Both the nanocomposites show higher vibrational energy dissipation compared to the pristine PE melt. Therefore, the underlying mechanism of viscous stress dissipation is due to the combined effect of PE and Gr in the nanocomposites.

Effect of Grafting on the Viscoelastic Behavior of the Stacked GO−PE Nanocomposite. A more versatile and promising GO nanofiller was studied to further investigate the impact of grafting. The viscoelastic behavior of GO with an approximate oxidation level of ≈70% is evaluated across four decades of frequencies, with varying grafting densities (0.55, 2.56, and 4.46) as depicted in Figure 12.

To assess the effect of grafting on the GO−PE nanocomposite, both G' and G'' were analyzed and also compared to the grafted Gr−PE system with a similar degree of grafting. Across the frequency range of 0.001−0.1 THz, G' and G'' displayed a similar pattern, with a log−log plot exhibiting an upward shift corresponding to the degree of grafting. At lower frequencies, the dominant factor influencing the upward shift in G' and G'' was the slow modes of polymer relaxation. As

https://doi.org/10.1021/acsomega.3c07690
ACS Omega 2024, 9, 9063−9075

more grafted chains exhibited slower relaxation than matrix chains, G'' was enhanced to a certain extent. The mobility of grafted chains was reduced, and the enthalpic interaction arising from GO often jammed the chains at the interface, thereby increasing the elasticity as seen in the upward shift in G'. Interestingly, at higher frequencies (>0.1 THz), faster relaxation modes and atomic vibrational modes influenced G' and G''. Multiple vibrational modes in GO and PE chains became more prominent, as depicted in Figure 12. Compared to graft-type GnP-PE, the grafted GO−PE system shows an insignificant effect on the storage modulus at lower frequencies in contrast to the loss modulus. Importantly, the frequency difference for the highest dissipation is observed to be filler-dependent. The grafted GnP−PE shows the highest energy dissipation at a higher frequency. At such high frequencies, the vibrational mode of the material leads to the majority of the shear dissipation, which was further supported by the VDOS spectra (shown in the dashed region) of GO for varying grafting densities, as shown in Figure 12. The frequency range 0−10 THz exhibited the highest vibrational energy for GO with the lowest grafting density and vice versa. The trend observed in the VDOS of GO strongly aligned with the energy dissipation characteristic of the GO−PE nanocomposite, as shown in the inset.

CONCLUSIONS

In this work, CG-MD simulations were carried out to study the effect of the polymer nanocomposite with and without grafting on the T_g and the mechanical and viscoelastic behavior of nacre-inspired polymer nanocomposites. The stacked nanocomposite was modeled by using three stacked Gr nanosheets incorporated in the PE matrix. With the introduction of stacked Gr, a notable increase (≈20 K) in the T_g was observed. This temperature enhancement was further amplified by grafting PE chains onto the Gr fillers. To comprehend this significant elevation in T_g, the study delved into the underlying molecular mechanisms, encompassing diffusion and time autocorrelation functions.

Furthermore, the mechanical performance of both ungrafted and grafted GnP−PE nanocomposites was explored. An elevation in stiffness and remarkable reinforcement were observed in the grafted GnP−PE nanocomposite. This stiffness and tensile strength improvement was attributed to the effective stress transmission between the PE matrix and the grafted Gr, thus resulting in superior mechanical properties for the graft-type nanocomposite. Nonequilibrium shear deformation simulations were carried out to study the frequency-dependent moduli of the nanocomposites. The system's viscoelastic behavior was analyzed over five decades of frequency. The dissipative behavior of the stacked and grafted GnP−PE is very sensitive to the deformation frequency. Strikingly, the grafted GnP−PE nanocomposite exhibited higher elastic and loss moduli, showing enhanced energy dissipation characteristics similar to nacre-like composites. The loss factor or tan δ of the composite was observed to be ≈ 25−35% higher than that of pristine PE. The enhanced stress transfer between the matrix and the filler was observed for the graft-type composite during the oscillating shear deformation, leading to efficient dissipation.

Additionally, a GO−PE composite was used to ascertain the effect of grafting on mechanical behavior. When considering smaller frequencies (below 0.1 THz), both the elastic modulus and the loss modulus exhibited a rise proportional to the degrees of grafting. The enhancement of the viscoelastic behavior is significantly influenced not only by the stiffness of GO but also by the relaxation of the PE chain. Conversely, at higher frequencies, specifically at the maximum shear dissipation frequency, the impact of grafting was validated by examining the vibrational mode of dissipation through the analysis of the VDOS. Prominent peaks were detected in Gr and GO, with GO showing slightly greater energy dissipation in the case of the lower grafting density composite.

These findings contribute to the swiftly growing realm of establishing connections between the structure and properties in high-performance nacre-inspired composites. It is foreseen that these simulation methods can be readily expanded to simulate a variety of microstructures existing in nature. This expansion aims to enhance mechanical attributes like strength, toughness, damping, and even responses to high-speed deformations such as impact[44,72] and shock loading.[73−75] As a result, these simulations could provide valuable guidance for the experimental design of such materials.

ASSOCIATED CONTENT

Supporting Information

The Supporting Information is available free of charge at https://pubs.acs.org/doi/10.1021/acsomega.3c07690.

Finite-size effect on GnP-PE composites' mechanical properties, physical properties of GnP−PE nanocomposites, effect of strain rate on tensile properties of the grafted GnP−PE system, and orientation dependence on viscoelastic behavior (PDF)

AUTHOR INFORMATION

Corresponding Author

Raghavan Ranganathan − *Department of Materials Engineering, Indian Institute of Technology Gandhinagar, Gandhinagar 382355, India;* orcid.org/0000-0003-1015-791X; Email: rraghav@iitgn.ac.in

Author

Param Punj Singh − *Department of Materials Engineering, Indian Institute of Technology Gandhinagar, Gandhinagar 382355, India;* orcid.org/0000-0002-8486-0838

Complete contact information is available at: https://pubs.acs.org/10.1021/acsomega.3c07690

Notes

The authors declare no competing financial interest.

ACKNOWLEDGMENTS

The authors acknowledge the support from IIT Gandhinagar's PARAM Ananta Supercomputer Facility for all the simulations reported in this work.

REFERENCES

(1) Marvila, M. T.; de Azevedo, A. R. G.; de Matos, P. R.; Monteiro, S. N.; Vieira, C. M. F. Materials for production of high and ultra-high performance concrete: Review and perspective of possible novel materials. *Materials* **2021**, *14*, 4304.

(2) Lin, R.-B.; Zhang, Z.; Chen, B. Achieving high performance metal-organic framework materials through pore engineering. *Acc. Chem. Res.* **2021**, *54*, 3362−3376.

(3) Mahmood, A.; Wang, J.-L. Machine learning for high performance organic solar cells: current scenario and future prospects. *Energy Environ. Sci.* **2021**, *14*, 90−105.

(4) Liang, S.-J.; Cheng, B.; Cui, X.; Miao, F. Van der Waals heterostructures for high-performance device applications: challenges and opportunities. *Adv. Mater.* **2020**, *32*, 1903800.
(5) Liu, A.; Liang, X.; Ren, X.; Guan, W.; Gao, M.; Yang, Y.; Yang, Q.; Gao, L.; Li, Y.; Ma, T. Recent progress in MXene-based materials: potential high-performance electrocatalysts. *Adv. Funct. Mater.* **2020**, *30*, 2003437.
(6) Chao, D.; Zhou, W.; Xie, F.; Ye, C.; Li, H.; Jaroniec, M.; Qiao, S.-Z. Roadmap for advanced aqueous batteries: From design of materials to applications. *Sci. Adv.* **2020**, *6*, No. eaba4098.
(7) Kuang, X.; Roach, D. J.; Wu, J.; Hamel, C. M.; Ding, Z.; Wang, T.; Dunn, M. L.; Qi, H. J. Advances in 4D printing: materials and applications. *Adv. Funct. Mater.* **2019**, *29*, 1805290.
(8) Choi, S.; Han, S. I.; Kim, D.; Hyeon, T.; Kim, D.-H. High-performance stretchable conductive nanocomposites: materials, processes, and device applications. *Chem. Soc. Rev.* **2019**, *48*, 1566−1595.
(9) Yuan, S.; Shen, F.; Chua, C. K.; Zhou, K. Polymeric composites for powder-based additive manufacturing: Materials and applications. *Prog. Polym. Sci.* **2019**, *91*, 141−168.
(10) Costa, J. C.; Spina, F.; Lugoda, P.; Garcia-Garcia, L.; Roggen, D.; Münzenrieder, N. Flexible sensors-from materials to applications. *Technologies* **2019**, *7*, 35.
(11) Sun, J.; Bhushan, B. Hierarchical structure and mechanical properties of nacre: a review. *RSC Adv.* **2012**, *2*, 7617−7632.
(12) Jia, H.; Li, Y.; Luan, Y.; Zheng, Y.; Yang, J.; Wang, L.; Guo, Z.; Wu, X. Bioinspired Nacre-like GO-based bulk with easy scale-up process and outstanding mechanical properties. *Composites, Part A* **2020**, *132*, 105829.
(13) Naveen, J.; Jawaid, M.; Goh, K. L.; Reddy, D. M.; Muthukumar, C.; Loganathan, T. M.; Reshwanth, K. N. G. L. Advancement in Graphene-Based Materials and Their Nacre Inspired Composites for Armour Applications-A Review. *Nanomaterials* **2021**, *11*, 1239.
(14) Ghazlan, A.; Ngo, T.; Tan, P.; Xie, Y. M.; Tran, P.; Donough, M. Inspiration from Nature's body armours−A review of biological and bioinspired composites. *Composites, Part B* **2021**, *205*, 108513.
(15) Perera, A. S.; Coppens, M.-O. Re-designing materials for biomedical applications: from biomimicry to nature-inspired chemical engineering. *Philos. Trans. R. Soc., A* **2019**, *377*, 20180268.
(16) Zhang, W.; Wei, L.; Ma, Z.; Fan, Q.; Ma, J. Advances in waterborne polymer/carbon material composites for electromagnetic interference shielding. *Carbon* **2021**, *177*, 412−426.
(17) Pruitt, L. A. Deformation, yielding, fracture and fatigue behavior of conventional and highly cross-linked ultra high molecular weight polyethylene. *Biomaterials* **2005**, *26*, 905−915.
(18) Knuuttila, H.; Lehtinen, A.; Nummila-Pakarinen, A. Advanced polyethylene technologies−controlled material properties. *Long Term Properties of Polyolefins*; Springer, 2004; Vol. *169*, pp 13−28.
(19) Zhang, Y.; Wang, Y.; Huang, Y.; Wan, Y. Preparation and properties of three-dimensional braided UHMWPE fiber reinforced PMMA composites. *J. Reinforc. Plast. Compos.* **2006**, *25*, 1601−1609.
(20) Zhu, Y.; Murali, S.; Cai, W.; Li, X.; Suk, J. W.; Potts, J. R.; Ruoff, R. S. Graphene and graphene oxide: synthesis, properties, and applications. *Adv. Mater.* **2010**, *22*, 3906−3924.
(21) Huang, X.; Yin, Z.; Wu, S.; Qi, X.; He, Q.; Zhang, Q.; Yan, Q.; Boey, F.; Zhang, H. Graphene-based materials: synthesis, characterization, properties, and applications. *Small* **2011**, *7*, 1876−1902.
(22) Asmatulu, R.; Khan, W. S.; Reddy, R. J.; Ceylan, M. Synthesis and analysis of injection-molded nanocomposites of recycled high-density polyethylene incorporated with graphene nanoflakes. *Polym. Compos.* **2015**, *36*, 1565−1573.
(23) Vasileiou, A. A.; Kontopoulou, M.; Docoslis, A. A noncovalent compatibilization approach to improve the filler dispersion and properties of polyethylene/graphene composites. *ACS Appl. Mater. Interfaces* **2014**, *6*, 1916−1925.
(24) Tan, Z.; Zhang, M.; Li, C.; Yu, S.; Shi, G. A general route to robust nacre-like graphene oxide films. *ACS Appl. Mater. Interfaces* **2015**, *7*, 15010−15016.
(25) Wu, Y.; Cao, R.; Ji, L.; Huang, W.; Yang, X.; Tu, Y. Synergistic toughening of bioinspired artificial nacre by polystyrene grafted graphene oxide. *RSC Adv.* **2015**, *5*, 28085−28091.
(26) Liu, L.; Gao, Y.; Liu, Q.; Kuang, J.; Zhou, D.; Ju, S.; Han, B.; Zhang, Z. High mechanical performance of layered graphene oxide/poly (vinyl alcohol) nanocomposite films. *Small* **2013**, *9*, 2466−2472.
(27) Putz, K. W.; Compton, O. C.; Palmeri, M. J.; Nguyen, S. T.; Brinson, L. C. High-nanofiller-content graphene oxide−polymer nanocomposites via vacuum-assisted self-assembly. *Adv. Funct. Mater.* **2010**, *20*, 3322−3329.
(28) Wan, S.; Peng, J.; Li, Y.; Hu, H.; Jiang, L.; Cheng, Q. Use of synergistic interactions to fabricate strong, tough, and conductive artificial nacre based on graphene oxide and chitosan. *ACS Nano* **2015**, *9*, 9830−9836.
(29) Cilento, F.; Martone, A.; Pastore Carbone, M. G.; Galiotis, C.; Giordano, M. Nacre-like GNP/Epoxy composites: Reinforcement efficiency vis-a-vis graphene content. *Compos. Sci. Technol.* **2021**, *211*, 108873.
(30) Park, S.; Dikin, D. A.; Nguyen, S. T.; Ruoff, R. S. Graphene oxide sheets chemically cross-linked by polyallylamine. *J. Phys. Chem. C* **2009**, *113*, 15801−15804.
(31) Safaei, M.; Sheidaei, A.; Baniassadi, M.; Ahzi, S.; Mosavi Mashhadi, M.; Pourboghrat, F. An interfacial debonding-induced damage model for graphite nanoplatelet polymer composites. *Comput. Mater. Sci.* **2015**, *96*, 191−199.
(32) Liu, Y.; Hamon, A.-L.; Bai, J. Directly measuring interfacial shear strength between Polymethyl methacrylate and graphene nanoplatelets. *Mater. Lett.* **2016**, *182*, 244−247.
(33) Fim, F. d. C.; Basso, N. R.; Graebin, A. P.; Azambuja, D. S.; Galland, G. B. Thermal, electrical, and mechanical properties of polyethylene−graphene nanocomposites obtained by in situ polymerization. *J. Appl. Polym. Sci.* **2013**, *128*, 2630−2637.
(34) Kim, H.; Kobayashi, S.; AbdurRahim, M. A.; Zhang, M. J.; Khusainova, A.; Hillmyer, M. A.; Abdala, A. A.; Macosko, C. W. Graphene/polyethylene nanocomposites: Effect of polyethylene functionalization and blending methods. *Polymer* **2011**, *52*, 1837−1846.
(35) Krishnamoorthy, K.; Veerapandian, M.; Yun, K.; Kim, S.-J. The chemical and structural analysis of graphene oxide with different degrees of oxidation. *Carbon* **2013**, *53*, 38−49.
(36) Lv, C.; Xue, Q.; Xia, D.; Ma, M. Effect of chemisorption structure on the interfacial bonding characteristics of graphene−polymer composites. *Appl. Surf. Sci.* **2012**, *258*, 2077−2082.
(37) Jin, Y.; Duan, F.; Mu, X. Functionalization enhancement on interfacial shear strength between graphene and polyethylene. *Appl. Surf. Sci.* **2016**, *387*, 1100−1109.
(38) Gaska, K.; Kádár, R.; Rybak, A.; Siwek, A.; Gubanski, S. Gas barrier, thermal, mechanical and rheological properties of highly aligned graphene-LDPE nanocomposites. *Polymers* **2017**, *9*, 294.
(39) Tang, L.-C.; Zhao, L.; Guan, L.-Z. 7 Graphene/Polymer Composite Materials: Processing, Properties and Applications. *Advanced Composite Materials: Properties and Applications*; Dimensions, 2017; pp 349−419.
(40) Verma, A.; Parashar, A.; Packirisamy, M. Effect of grain boundaries on the interfacial behaviour of graphene-polyethylene nanocomposite. *Appl. Surf. Sci.* **2019**, *470*, 1085−1092.
(41) Alian, A.; Dewapriya, M.; Meguid, S. Molecular dynamics study of the reinforcement effect of graphene in multilayered polymer nanocomposites. *Mater. Des.* **2017**, *124*, 47−57.
(42) Yuan, Z.; Lu, Z.; Yang, Z.; Sun, J.; Xie, F. A criterion for the normal properties of graphene/polymer interface. *Comput. Mater. Sci.* **2016**, *120*, 13−20.
(43) Parashar, A.; Mertiny, P. Multiscale model to study of fracture toughening in graphene/polymer nanocomposite. *Int. J. Fract.* **2013**, *179*, 221−228.
(44) Liu, N.; Pidaparti, R.; Wang, X. Mechanical performance of graphene-based artificial nacres under impact loads: a coarse-grained molecular dynamic study. *Polymers* **2017**, *9*, 134.

https://doi.org/10.1021/acsomega.3c07690
ACS Omega 2024, 9, 9063−9075

(45) Chaurasia, A.; Jalan, S. K.; Parashar, A. An atomistic approach to study the dynamic and structural response in 2D nanofiller reinforced polyethylene nanocomposites under ultra-short shock pulse loading. *Mech. Mater.* **2022**, *169*, 104305.
(46) Dewapriya, M.; Meguid, S. Comprehensive molecular dynamics studies of the ballistic resistance of multilayer graphene-polymer composite. *Comput. Mater. Sci.* **2019**, *170*, 109171.
(47) Bowman, A.; Roth, M.; Lawrimore, W.; Newman, J. Graphene Confined Polymer Thin Films Subjected to Supersonic Impact. In *ASME International Mechanical Engineering Congress and Exposition*, V012T12A014; ASME, 2021.
(48) Plimpton, S. Fast parallel algorithms for short-range molecular dynamics. *J. Comput. Phys.* **1995**, *117*, 1−19.
(49) Stukowski, A. Visualization and analysis of atomistic simulation data with OVITO−the Open Visualization Tool. *Modell. Simul. Mater. Sci. Eng.* **2009**, *18*, 015012.
(50) Ruiz, L.; Xia, W.; Meng, Z.; Keten, S. A coarse-grained model for the mechanical behavior of multi-layer graphene. *Carbon* **2015**, *82*, 103−115.
(51) Wei, X.; Meng, Z.; Ruiz, L.; Xia, W.; Lee, C.; Kysar, J. W.; Hone, J. C.; Keten, S.; Espinosa, H. D. Recoverable slippage mechanism in multilayer graphene leads to repeatable energy dissipation. *ACS Nano* **2016**, *10*, 1820−1828.
(52) Tschopp, M.; Bouvard, J.-L.; Ward, D.; Horstemeyer, M. Atomic scale deformation mechanisms of amorphous polyethylene under tensile loading. *Supplemental Proceedings: Materials Fabrication, Properties, Characterization, and Modeling*; Wiley, 2011; Vol. *2*, pp 789−794.
(53) Xie, F.; Lu, Z.; Yang, Z.; Hu, W.; Yuan, Z. Mechanical behaviors and molecular deformation mechanisms of polymers under high speed shock compression: a molecular dynamics simulation study. *Polymer* **2016**, *98*, 294−304.
(54) Lorentz, H. A. Ueber die Anwendung des Satzes vom Virial in der kinetischen Theorie der Gase. *Ann. Phys.* **1881**, *248*, 127−136.
(55) Meng, Z.; Soler-Crespo, R. A.; Xia, W.; Gao, W.; Ruiz, L.; Espinosa, H. D.; Keten, S. A coarse-grained model for the mechanical behavior of graphene oxide. *Carbon* **2017**, *117*, 476−487.
(56) Ranganathan, R.; Shi, Y.; Keblinski, P. Commonalities in frequency-dependent viscoelastic damping in glasses in the MHz to THz regime. *J. Appl. Phys.* **2017**, *122*, 145103.
(57) Ranganathan, R.; Shi, Y.; Keblinski, P. Frequency-dependent mechanical damping in alloys. *Phys. Rev. B* **2017**, *95*, 214112.
(58) Li, T.; Meng, Z.; Keten, S. Interfacial mechanics and viscoelastic properties of patchy graphene oxide reinforced nanocomposites. *Carbon* **2020**, *158*, 303−313.
(59) Evans, D. J.; Morriss, G. Nonlinear-response theory for steady planar Couette flow. *Phys. Rev. A* **1984**, *30*, 1528−1530.
(60) Daivis, P. J.; Todd, B. A simple, direct derivation and proof of the validity of the SLLOD equations of motion for generalized homogeneous flows. *J. Chem. Phys.* **2006**, *124*, 194103.
(61) Thompson, A. P.; Plimpton, S. J.; Mattson, W. General formulation of pressure and stress tensor for arbitrary many-body interaction potentials under periodic boundary conditions. *J. Chem. Phys.* **2009**, *131*, 154107.
(62) Gao, Y.; Liu, J.; Shen, J.; Zhang, L.; Guo, Z.; Cao, D. Uniaxial deformation of nanorod filled polymer nanocomposites: a coarse-grained molecular dynamics simulation. *Phys. Chem. Chem. Phys.* **2014**, *16*, 16039−16048.
(63) Kalathi, J. T.; Kumar, S. K.; Rubinstein, M.; Grest, G. S. Rouse mode analysis of chain relaxation in homopolymer melts. *Macromolecules* **2014**, *47*, 6925−6931.
(64) Peng, W.; Ranganathan, R.; Keblinski, P.; Ozisik, R. Viscoelastic and dynamic properties of well-mixed and phase-separated binary polymer blends: A molecular dynamics simulation study. *Macromolecules* **2017**, *50*, 6293−6302.
(65) Singh, P. P.; Ranganathan, R. Tensile and viscoelastic behavior in nacre-inspired nanocomposites: a coarse-grained molecular dynamics study. *Nanomaterials* **2022**, *12*, 3333.
(66) Frigo, M.; Johnson, S. G. FFTW: An adaptive software architecture for the FFT. *Proceedings of the 1998 IEEE International Conference on Acoustics, Speech and Signal Processing, ICASSP'98 (Cat. No. 98CH36181)*; IEEE, 1998; pp 1381−1384.
(67) Gonçalves, S.; Bonadeo, H. Vibrational densities of states from molecular-dynamics calculations. *Phys. Rev. B: Condens. Matter Mater. Phys.* **1992**, *46*, 12019−12021.
(68) Stehling, F. C.; Mandelkern, L. The glass temperature of linear polyethylene. *Macromolecules* **1970**, *3*, 242−252.
(69) Han, J.; Gee, R. H.; Boyd, R. H. Glass transition temperatures of polymers from molecular dynamics simulations. *Macromolecules* **1994**, *27*, 7781−7784.
(70) Peng, W.; Ranganathan, R.; Keblinski, P.; Akcora, P.; Ozisik, R. Viscoelastic and dynamic properties of polymer grafted nanocomposites with high glass transition temperature graft chains. *J. Appl. Phys.* **2019**, *126*, 195102.
(71) Hossain, D.; Tschopp, M. A.; Ward, D.; Bouvard, J.-L.; Wang, P.; Horstemeyer, M. F. Molecular dynamics simulations of deformation mechanisms of amorphous polyethylene. *Polymer* **2010**, *51*, 6071−6083.
(72) Peng, C.; Tran, P. Bioinspired functionally graded gyroid sandwich panel subjected to impulsive loadings. *Composites, Part B* **2020**, *188*, 107773.
(73) Ha, N. S.; Lu, G. A review of recent research on bio-inspired structures and materials for energy absorption applications. *Composites, Part B* **2020**, *181*, 107496.
(74) Sen, D.; Buehler, M. J. Shock loading of bone-inspired metallic nanocomposites. *Solid State Phenom.* **2008**, *139*, 11−22.
(75) Singh, P. P.; Ranganathan, R. Superior Protection Conferred by Multi-Layered Graphene−Polyethylene Nanocomposites under Shock Loading. *ACS Appl. Eng. Mater.* **2023**..

https://doi.org/10.1021/acsomega.3c07690
ACS Omega 2024, 9, 9063−9075